Millimetric spatial resolution time-expanded ϕ-OTDR

Miguel Soriano-Amat[1,2,*], Phillipe Guay[2], Hugo F. Martins[3] , Sonia Martin-Lopez[1], Miguel Gonzalez-Herraez[1], María R. Fernández-Ruiz[1] and Jerome Genest[2]

[1]*Universidad de Alcalá, EPS, 28805 Madrid, España*
[2]*Centre d'optique, photonique et laser, Université Laval, Québec, QC, G1V 0A6, Canada*
[3]*Instituto de Óptica "Daza de Valdés" IO-CSIC, C/Serrano 121, 28006 Madrid, Spain*
*Corresponding author: miguel.soriano@uah.es

Abstract

Time-expanded phase OTDR is a distributed optical fiber sensing technology based on dual-frequency combs that allows performing dynamic and high spatial resolution measurements while maintaining reduced detection requirements. Since the formalization of the technique, different experimental schemes have been satisfactorily tested, with a general performance of cm-scale spatial resolution over hundreds of meters. In this article, we present an optimized scheme with enhanced energy and spectral efficiencies that allows reaching 5 mm spatial resolution. As compared to previous experimental approaches, the presented architecture is based on a free-running dual comb setup generated through pure electro-optical phase modulation. Besides, the introduction of an optical hybrid in the detection stage allows for doubling the spatial resolution while keeping the refresh rate and the sensing range unchanged.

Introduction

Distributed optical fiber sensors (DOFS) based on Rayleigh backscattering stand out as cost-effective solutions to monitor, in real time, structures that require a large number of interrogating points [1]. One variant of this kind of DOFS is phase-sensitive optical time-domain reflectometry (ϕOTDR). This technique relies on the analysis of the Rayleigh backscattering signal generated when a coherent pulse is launched to the fiber under test (FUT). Normally, these schemes attain a sensing range of tens of kilometers with resolutions of several meters, i.e., offering around 10,000 virtual sensing points [1–3]. Besides, the acoustic sampling of these systems can easily reach the kHz scale, since it is limited only by the length of the fiber. The metric-scale spatial resolution is imposed by the need of reaching sufficiently high signal-to-noise ratio (SNR) in the retrieved traces. Different solutions have been explored to improve the spatial resolution, such as pulse coding or pulse compression techniques [4,5]. However, the associated spreading of the pulse bandwidth involves the need for high-speed photodetectors, with a consequent growth of the noise and of the required data rate. The latter additionally entails an important increment of the computing requirements for the retrieval of the perturbations.

In contrast, interrogators based on Rayleigh optical frequency domain reflectometry (OFDR) can readily attain a remarkable spatial resolution in the mm or μm scale over lengths of tens of meters [6]. Such performance is achieved by the introduction of a large frequency sweep in the probe light. However, the sweeping operation requires a high degree of linearity without mode-hopping. Existing nonlinearities are normally compensated thanks to an auxiliary interferometer that measures the instantaneous frequency [7]. Different OFDR approaches have been developed to increase the sensing range and interrogation speed, but generally at the cost of degrading the spatial resolution to values close to typical in ϕOTDR techniques [8,9].

Recently, a high-resolution ϕOTDR scheme based on dual-frequency comb (DFC) signals was proposed [10]. One comb is sent through the FUT, and the produced Rayleigh backscattering is coherently detected by multi-heterodyning with the other comb acting as local oscillator. This technique, called time expanded (TE-)ϕOTDR, enables to interrogate fibers up to the kilometer range while maintaining a resolution in the order of cm and low-bandwidth electronics at the detection stage [11]. To date, the most extended TE-ϕOTDR architecture relies on a high-performance arbitrary waveform generator (AWG) to create the optical combs. The combs are generally spectrally phase-coded to avoid the formation of short pulses, hence increasing the SNR of the traces. Such spectral coding is automatically decoded in detection whenever the pair of combs shares the same phase profile [11]. Despite the elevated performance exhibited and the flexibility to configure the combs shown by this approach, both the cost and complexity of the resulting system prevent its integration into a field-deployable system. A few solutions have been proposed to

solve this drawback. One of them is based on step-recovery diodes to generate the frequency combs [12]. Using this technique, measurements with 3 cm spatial resolution were reported by only using low frequency electronics both in the comb generation and detection stages (i.e., no more than 10 MHz). Despite the simplicity of the system, step-recovery diodes produce nearly transform-limited train of pulses, which ultimately limits the SNR and, as a consequence, the attainable sensing range and the maximum acoustic frequency.

Another proposal to simplify the TE-ϕOTDR scheme replaces the AWG by a couple of commercial pseudo-random bit sequence (PRBS) generators designed for telecommunications [13]. In the proof-of-concept, the authors reported 1 cm spatial resolution measurements over FUTs of hundreds of meters. Despite achieving good performance in terms of sensing points, both the energy and spectral efficiency of the scheme are highly constrained. In particular, in the configuration proposed in [13], the two optical combs were generated over the same optical carrier via an electro-optical intensity modulation process. Since the PRBS boards produce a non-return-to-zero (NRZ) binary pattern, the comb's spectral envelope has a sinc-like shape. To ensure unambiguous down-conversion when detecting the beating between the Rayleigh-backscattering and local oscillator combs, at least half of the optical spectrum must be filtered out. Yet, considering the width of the transition bands of the optical filter, more than half of the spectrum is eventually filtered out, including part of the lines with higher energy (i.e., those closer to the carrier frequency). Besides, the features of the commercial PRBS boards impose an elevated number of sensing points, heavily restricting the flexibility in the selection of the sensing performance, and generally limiting the attainable acoustic sampling to a few Hz.

In this work, we explore the possibility to increase the flexibility and performance by leveraging some solutions already deployed in other DFC-based fields such as dual comb spectroscopy. Among the implemented improvements, we have generated a pair of free-running combs achieving a high degree of post-processed mutual coherence thanks to the application of a self-correcting algorithm that compensates for the relative frequency fluctuations of the combs [14–16]. We have optimized the energy efficiency through the generation of the combs by electro-optical phase modulation of a carrier with PRBS. Additionally, an optical hybrid is employed in detection, avoiding the need for filtering part of the optical spectrum, with a twofold increase in the spectral efficiency of the detection process [17,18]. The use of an optical hybrid has already been employed in conventional ϕ-OTDR to increase the spectral efficiency in two-fold [19]. To date, the PRBS approach seems to be the most promising solution for implementing an embeddable interrogator in TE-ϕOTDR. Here, the PRBS are generated using a gigabit transceiver (GTX) included in the field-programmable gate arrays (FPGA) evaluation board. This equipment permits the selection of sequences of arbitrary length and therefore, offering better tunability in the selection of the sensing performance than that obtained with commercially available PRBS boards. The combination of these improvements yields the first TE-ϕOTDR scheme that reaches millimeter resolution using electronics within the MHz range for detection while maintaining an excellent sensitivity, as proved in the here shown experimental tests. This way, we are reaching spatial resolution typically achieved by Rayleigh OFDR systems but offering at the same time longer measuring ranges and higher measurement update rates. Furthermore, the proposed system avoids the need for a tunable laser or an auxiliary interferometer to compensate laser frequency sweeping non-linearities. On the other hand, note that inelastic-scattering approaches are neither capable of reaching such level of position precision, nor performing real-time, acoustic measurements [20,21]. For these reasons, we believe that the performance shown by the TE-ϕOTDR presented in this work may be of interest in different areas like robotics, aeronautic structures, transportation means, etc.

Optimization of the generation and detection scheme

We start here with a description of the generation and detection stages of the presented TE-ϕOTDR architecture. For this development, we have considered different optimization approaches normally applied in the fields of optical spectroscopy and optical communications. The proposed OFC generation scheme relies on an electro-optical (EO) phase modulator driven by an FPGA[22]. This FPGA continuously reproduces an arbitrary PRBS sequence previously computed offline. Then it is possible to use maximum length sequences (MLS) to maximize the spectral smoothness of the generated OFC. However, the main advantage of employing an FPGA is the tunability in the selection of the sequence length. In particular, for a given bit duration (τ_{bit}, fixed by an external reference), the attainable sensing range of the system can be tuned as:

$$L_{fiber} = \frac{c}{2n} \cdot (2^m - 1) \cdot \tau_{bit} \qquad (1)$$

being c the speed of light in a vacuum, n the effective refractive index of the optical fiber and m the bits involved in the generation of a PRBS sequence of length N = $(2^m - 1)$.

On the other hand, the generation of optical combs based on phase modulation (PM) of a carrier driven by PRBS has been previously demonstrated as a flexible and energy efficient approach for EO comb generation [16]. The employment of phase modulation leads to a reduction of the peak-to-average power ratio (PAPR) of the optical signals to practically 0 dB. As demonstrated in previous work, the PAPR of the signals has a direct impact on the SNR improvement of the retrieved traces [23]. When the PRBS signals are adjusted to reach Vπ on the PM, the resulting modulated spectrum is composed of two complex-conjugated sidebands around the optical carrier, ν_0 (Fig. 1a)). When working with a DFC, it is important to ensure that the

interference between any pair of optical comb lines produces a beat note of unique frequency. Otherwise, the down-converted lines would suffer a spectral aliasing process upon photodetection. This effect is typically observed when the DFC is generated electro-optically with a single intensity or phase modulator (per comb). In this case, the DFC spectrum presents a symmetry around the central line of the two combs, which is located at the frequency of the modulated optical carrier (see Fig. 1. a). Different approaches can be employed to prevent the overlapping of information, depending on the type of coherent detection employed.
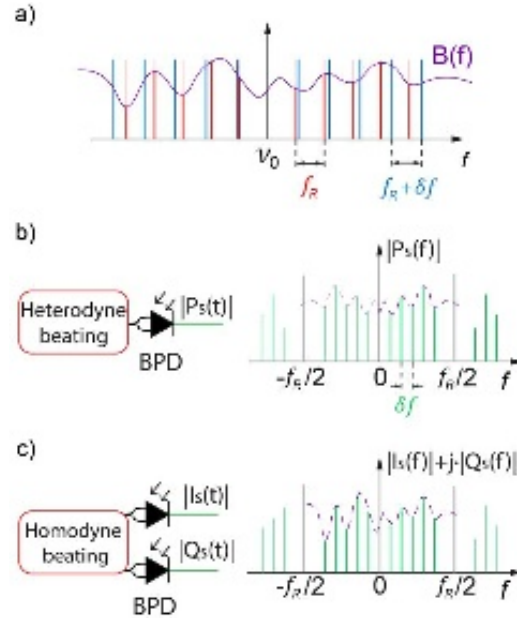

Figure 1 a) Dual frequency combs composed of a frequency comb of line spacing f_R and $f_R + \delta f$ (in red and blue, respectively), interrogating a sample with an frequency response given by B(f). The down-converted spectrum when employing heterodyne and homodyne detection approaches is shown in b) and c) respectively. $P_s(t)$ ($P_s(f)$) refers to the detected power as a function of time (frequency) in a heterodyne scheme, while $I_s(t)$ and $Q_s(t)$($I_s(f)$ and $Q_s(f)$) are the temporal (spectral) variations of the power obtained at the in-phase and quadrature branches, respectively.

In the heterodyne approach, both OFCs are directly combined and detected with a single photodetector. To prevent the information overlapping, each RF line must come from a unique beating between two different pairs of optical lines. This goal can be addressed by optically filtering one sideband [11] or by inducing a frequency shift over the OFC, e.g., using an acousto-optic modulator (AOM) [24,25]. This detection strategy involves measuring a single real-valued dataset, so the spectrum is symmetric around the origin (see the down-converted lines in Fig. 1.b)). Then, after a proper low-pass filtering, the effective RF spectral band in which the comb lines are located is $[0, f_R/2]$, where f_R is the repetition rate of one of the OFCs [11]. Taking into account all these restrictions, the condition to ensure the non-aliased down-converted OFC is given by:

$$(\delta f)_{Het} < \frac{f_R^2}{2B_{Opt}} \tag{2}$$

being B_{Opt} the effective optical bandwidth and δf the slight detuning of the line spacing between the two involved combs.

The spectral efficiency can be increased by including an optical hybrid (OH) in the detection scheme (i.e., a homodyne scheme). In this case, two balanced photodetectors retrieve separately the (real-valued) in-phase (I) and quadrature (Q) signals resulting from the beating between the two combs. Then, the information can be suitable mixed afterwards to obtain a non-aliased complex-valued waveform (the spectrum is no longer symmetrical around $f = 0$, as shown in Fig. 1.c). This approach directly doubles the attainable spectral resolution for a given DFC configuration. Furthermore, as now the beating lines can be distributed along the interval $[-f_R/2, f_R/2]$, the requisite to prevent aliasing when the interference signal is:

$$(\delta f)_{Hom} < \frac{f_R^2}{B_{Opt}} \tag{3}$$

Note that for the same δf and f_R values, the homodyne detection allows doubling the achievable optical bandwidth. More importantly, as no optical lines have to be suppressed, the filtering requirements are notably relaxed, i.e., now only employed for reducing noise by filtering amplified spontaneous emission (ASE). However, it is worth mentioning the necessity to calibrate relative amplitude and phase of the OH (to correctly recover the complex-valued information) and the additional optical losses introduced by this particular detection scheme. Furthermore, homodyne detection requires doubling the components at the detection stage. However, the cost of including a second digitizer and photodetector of a few MHz of bandwidth is more cost-effective than upgrading the generation scheme, whose typical bandwidths are in the 10 GHz scale.
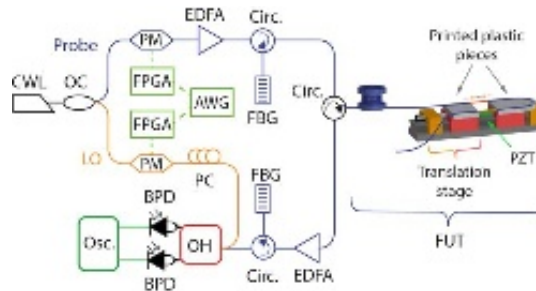
Experimental Setup

Figure 2 a) Experimental setup employed for the demonstration b) Design of the mechanism to induce small longitudinal elongations over a section of the FUT. OC: optical coupler. PC polarization controller.

For the experimental demonstration, we employed the setup shown in Fig. 2. The light emitted by a narrow linewidth continuous-wave laser (CWL) seeds two independent phase modulators (PM). The modulation signal is generated by two independent FPGA boards (Xilinx Virtex 7 FPGA VC707). Each board produces a customized maximum length PRBS with a user-defined length. Both probe and LO combs must be generated using PRBS with the same length and the same seed. Hence, we are introducing the same spectral phase profile in the comb lines, enabling an automatic decoding of the beatnotes placed at the first Nyquist zone. To generate two combs with different repetition rates, each FPGA receives a slightly detuned reference clock coming from the same arbitrary waveform generator (AWG). It should be noticed that this AWG only generates a low-frequency signal corresponding with the target comb line spacing (around 200 MHz). Note that other simpler equipment (but with enough accuracy to set a suitable frequency offset) could be employed. For example, previous iterations of this DFC generators use a direct digital synthesizer (DDS) evaluation board with a single frequency generator of tens of MHz as the reference clock[16]. Inside the FPGA, the GTX driver sends 50 bits at each clock signal, reaching a bit rate of 10 GHz. Compared to the first TE-ϕOTDR implementation based on PRBS sequences [13], this is a remarkable reduction –50-fold– of the clock generation requirements. Some parameters related to the shape of the bits (pre-emphasis and post-emphasis) can be controlled to optimize the envelope of the OFC spectrum. After modulation, the probe comb (i.e., the OFC that proves the spectral response of the FUT) is boosted by a high-power erbium-doped fiber amplifier (HP-EDFA) to increase the backscattering signal. The signal is filtered out by means of a fiber Bragg grating (FBG) to reduce the ASE. Then, the probe signal is launched to the FUT through an optical circulator (Circ.). The backscattered signal is amplified and filtered by another HP-EDFA and an FBG, respectively. Both FBGs have a bandwidth of 50 GHz centered on the laser wavelength. To recover the complex-valued information, both interferometer branches are combined in an OH. The resulting differential optical signals are sent to a couple of balanced photodetectors (BPD). The electrical signals are digitized by a digital oscilloscope (Osc.), which is not synchronized with the comb generators. Therefore, the recovered signals have to be post-processed to compensate for the lack of temporal mutual coherence caused by the relative temporal drift between the reference clocks [14]. From the recovered data, the algorithm segments the acquisition by interferograms and extracts the information of the phase changes that provoke frequency shifting and stretching in the down-converted lines. The correction includes a resampling of the interferograms. According to the Nyquist theorem, the program can compensate for frequency fluctuations in the interval defined by [0, $\delta f /2$]. Since the correction is based exclusively on the experimental data, the algorithm is called *self-correction*. This strategy to compensate for non-linearities in the waveform sampling prevents introducing a second interferometer (typically included in OFDR systems), thus increasing the stability of the experimental setup. In addition, the post-processing stage also takes into account the non-ideal behavior of the OH, thus correcting the unbalanced terms. Compared to other solutions used to compensate for sampling non-linearities (like external interferometers, typically used in OFDR systems),

the self-correction algorithm enhances the temporal stability, since allows correcting the path changes of the interferometer used to recover the backscatter information.

To generate a controlled small perturbation at the sub-cm scale, a customized tailor-made assembly is designed (sketched at the right part of Fig. 2). To produce longitudinal elongation over two size-controlled points (see FUT sections in orange), a couple of translation stages are mounted over an optical rail. Each stage is composed of a pair of metallic pieces, depicted in red and ocher, connected by a micrometer screw. In turn, both stages are connected by a commercial piezo-electric transducer (PZT), which is depicted in green within the perturbation mechanism in Fig. 2. As one of the stages is fixed to the rail, the other stage moves accordingly to the electrical signal employed to feed the PZT. This movement is transferred to a section of the FUT by a tailor-made plastic 3D printed component. The plastic pieces have a cleavage to allocate the fiber around the stressed points. The fiber is glued to the plastic pieces to improve the strain transfer. Besides, the glue helps to mechanically isolate the fiber at non-perturbed optical fiber sections*,* hence avoiding any force or movement on the non-perturbed fiber region. Furthermore, this perturbation system allows for demonstrating the possibility of monitoring different stress points along the FUT and verifying the distributed capabilities of the proposed system.

Experimental results

The proposed system has been experimentally validated by performing a series of distributed sensing measurements. In the first trial, the generation of the PRBS sequence involves m = 13 bits, so the sequence length is 8191. The reference clock that feeds the FPGA in charge of generating the probe comb emits a sinusoidal signal at 200 MHz while the FPGA associated with the LO comb is referenced to a sine wave at 199.988532 MHz. The line spacing of the probe comb is $f_R = \frac{1}{N \cdot \tau_{bit}} \approx 1.22$ MHz, enough to measure up to 84.091 m of fiber. Considering the number of comb lines and the GTX conversion factor, the small detuning between the comb line spacing is then 70 Hz, which implies that the first Nyquist zone (i.e., the frequency interval from 0 to $f_R/2$) is filled up to 94%. The reference clock sent to the FPGA that reproduces the LO signal has to be tuned with Hz precision to get that δf value. The board's output voltage and the gain of the RF amplifiers are adjusted so that the sequence reaches a peak-to-peak voltage value of $\sim V_\pi$, thus creating two sideband combs composed of 16381 lines. As the total optical bandwidth is 20 GHz, the nominal spatial resolution is 5 mm. This DFC is employed to interrogate a FUT of 55.475 m length, where two points of 5 mm length are mechanically disturbed. A set of five non-consecutive Rayleigh backscatter traces obtained with this configuration is shown in Fig. 3.a to show SNR and repeatability.
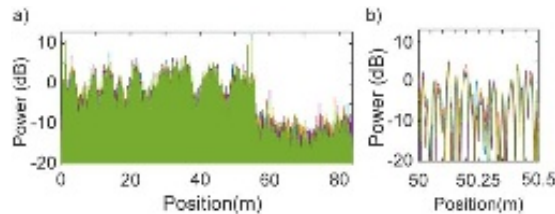

Figure 3 a) Set of five non-consecutive backscattered traces. b) Detailed section to verify the temporal stability among the recovered traces.

The length of the recovered backscatter trace matches the expected value, which confirms that the self-correction algorithm can compensate for the phase fluctuations related to the lack of synchronization between the detection and generation stages. Note that such fluctuations would lead to an incorrect estimation of the time-of-flight of the probe signal inside the fiber, and then, the position of each sensing point. Visually, the good temporal stability trace to trace can be observed in Fig. 3.b. Quantitatively, such stability is reflected in the SNR values. In this study, the SNR is calculated as the average of the SNR obtained across the different points. At each sensing point, the SNR is estimated as the ratio between the mean value of the temporal evolution of the power at each point (i.e., the signal term) and the variance of the temporal evolution of the power in the mentioned point (the noise term). This way, a temporal jitter will diminish the SNR level. The estimated SNR for this configuration is 12 dB. Both the figure and the SNR values confirm the capabilities of the self-correction algorithm to reinforce the mutual coherence between OFCs since no physical synchronization is performed between the generation and detection schemes. This algorithm also corrects the fluctuations in the duration of each trace, forcing that each backscattered signal is composed of the same integer number of samples.

The first step to retrieve the strain information is extracting the phase profile from the complex-valued backscattered traces. The phase profile recovered from the first trace is subtracted from the rest of the dataset to recover the relative phase changes induced by the perturbations. Hence, these traces are spatially differentiated (considering a gauge length of 5 mm) to localize the position of the different events in the fiber. The trace-to-trace phase difference is directly proportional to the strain perturbation [11], allowing us to obtain the evolution of the strain around the disturbed points, shown in Fig. 4 a).
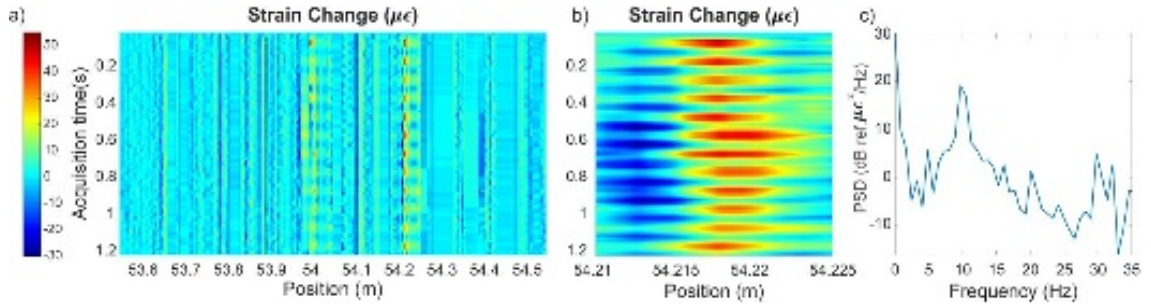
Figure 4 a) 3D strain map around the pertubated region b) Detail of one of the induced perturbation c) Power spectral denisity obained at a representative disturbed position (54.217m).

As observed, a couple of synchronized disturbed points are recovered. The detailed section of one of such points (Fig. 4 b) highlights both the matching to the attainable spatial resolution (5 mm) and a good temporal stability trace to trace. The application of a high-pass filter (with a cutoff frequency of 5 kHz) to detected RF comb signal prevents the effect of the low-frequency noise contributions to the temporal stability between traces. The measured strain values cover a range of 50 $\mu\epsilon$, while the accuracy is estimated at 2.4 $\mu\epsilon$ (0.12 rad). The phase estimation at the fading points is performed according to the nearest neighbor analysis [26]. The power spectral density (PSD) values obtained in a representative disturbed point is shown in Fig. 4.c. The high-order harmonics are considerably attenuated, proving the linearity of the perturbation setup. While the peak power of the component at the perturbation frequency is around 19.1 dB ref. $\mu\epsilon^2/Hz.$, the noise floor between 22 Hz and 35Hz is estimated at -7.4 dB ref. $\mu\epsilon^2/Hz$.

A second experimental demonstration entailed the employment of a PRBS sequence with length of 16383 (m = 14). Since the involved bandwidths are the same (B_{Opt} = 20 GHz), the increase of the number of sensing points has a direct impact on the sensing range (reaching 168.176 m, corresponding to $f_R \approx 610$ kHz) while maintaining the sub-centimeter spatial resolution (5 mm). However, the acoustic sampling is decreased to 18 Hz, which entails that the first Nyquist zone is filled up to 96.7% of its capacity. The reference clock of the probe comb is kept at 200 MHz, and now the second reference clock is set at 199.994102 MHz. As before, we show in Fig. 5.a a set of non-consecutive recovered traces. In this case, the FUT has a length of 135.685 m.
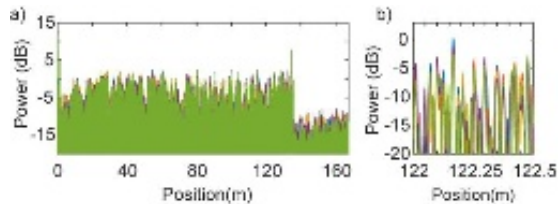

Figure 5 a) Set of non-consecutive backscattered traces. b) Detailed section to verify the temporal stability among the recovered traces.

The trace-to-trace stability is maintained even in such low refresh rates, standing out the capabilities of the employed self-correction algorithm. The SNR of the traces is 11.3 dB. The obtained SNR is approximately the same than in the previous case in spite of the reduction of δf (which, in principle, increases the SNR) [11]. One of the reasons is the fact that measurements with m=14 were digitized with half of the sampling rate than those with m =13 to maximize the acquisition time. This reduces by 3 dB the processing gain due to the lower oversampling. A set of traces digitalized at the same speed as m=13 returns an SNR improvement of the order of 2 dB. The second reason is that the post-processing algorithm used to compensate for the lack of synchronization between the generation and detection systems only corrects clock fluctuations of the order of $\delta f/2$. Then, the

reduction of the acoustic sampling leads to a degradation of SNR since the noise power term is increased. This effect is also noticed in the accuracy of the measurements since it is slightly lower than reported in the previous measurements (0.18 rad, 3.7 $\mu\epsilon$).
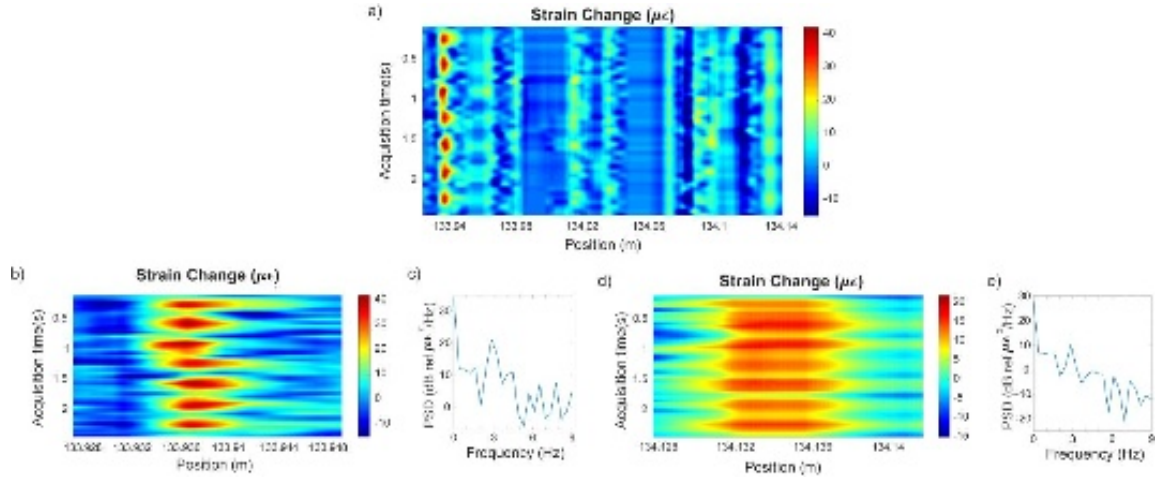

Figure 6 a) 3D strain map around the perturbed region. A zoom-in view of the induced perturbations around 133.936 m and 134.134 in b) and d). Power spectral density obtained in representative disturbed points are shown in c) and d) at the mentioned positions, respectively.

The retrieved strain maps around the perturbed points are shown in Fig. 6.b and d. A couple of 5 mm length sections of fiber are mechanically disturbed at 3 Hz. Although showing higher strain variations, the alignment at the point placed around 133.938m is worse than 134.134 m. This effect is partially related to the down-converted optical low-frequency noise. Besides, this noise also induces distortions in the position location. However, the high-pass filter cut-off frequency cannot be excessively increased to prevent a degradation of the spatial resolution. The strain range measured is around 40 $\mu\epsilon$. Given the weakness of the perturbation shown in Fig 6. d, we have intentionally clipped the maximum strain values in the mentioned figure to facilitate the visualization. The asymmetry in the strain values recovered at the disturbed points can be produced by small misalignments between the PZT, the stages and the 3D plastic pieces. This effect is also visible in the PSD values of both perturbations (Fig 6.c and e). As observed, the stronger perturbation has a peak at 3 Hz of 21.1 dB ref. $\mu\epsilon^2/Hz$, while the amplitude of the second disturbed point is 10.2 dB ref. $\mu\epsilon^2/Hz$. The noise floor, calculated as the median of the PSD values between 5 Hz and 9 Hz, has been estimated to be -1.5 dB ref. $\mu\epsilon^2/Hz$ and -7.5 dB ref. $\mu\epsilon^2/Hz$ for the mentioned perturbations, respectively.

Conclusions

In summary, in this work, we have implemented different solutions explored in the dual comb spectroscopy field to increase the energy and spectral efficiency of a TE-φOTDR-based sensor. In this technique, the sensing range is limited by the comb line spacing leading to relatively short distances of a few hundreds of meters. Despite that, the SNR of the traces is practically constant along the trace, not being a critical limitation for the achievable range as in traditional φOTDR schemes. Nevertheless, it is clear that, as in any other phase-demodulation φOTDR approach, the SNR is strongly linked to the sensitivity and to the impact of fading points in the perturbation recovery [27]. The implementation of the interrogator here proposed attains an optimized energy efficiency, since (i) the combs are generated via phase-modulation, which implies a PAPR equal to 0 dB in the probe and LO periodic sequences, and (ii) the use of an optical hybrid avoids the filtering of part of the available spectrum. Additionally, as compared with other experimental schemes, the inclusion of an optical hybrid in detection allows doubling the spatial resolution while maintaining the sensing range and the acoustic sampling. This improvement, along with the employment of a high-performance FPGA, allows recovering dynamically two separated perturbations with 5 mm spatial resolution. The proposed system enables the selection of the PRBS sequence length, thus adding a degree of freedom in the selection of the sensor performance, required to be integrated into a portable interrogator. Finally, for the first time in a TE−φ OTDR scheme, we include a post-processing algorithm (self-correction) to improve the mutual coherence between the probe and LO comb. This algorithm also corrects the length variability of the backscattered traces, facilitating the information recovery of each position

channel. Furthermore, the employment of the self-correction algorithm relaxes the requirements of synchronization and/or control systems, simplifying the interrogator structure. We believe the here proposed TE-ϕOTDR architecture is close to an optimal scheme for the implantation of low-cost, highly efficient and potentially embeddable interrogator.

FUNDING

Acknowledgments.

Disclosures. The authors have no conflicts to disclose.

Data availability. Data underlying the results presented in this paper are not publicly available at this time but may be obtained from the authors upon reasonable request.

Contributions

Conceptualization formal analysis and theoretical framework: M.S.-A. and J.G. Methodology: M.S.-A., P.G and J.G. Experimental work: M.S-A. and P.G Software: M.S-A, H.M, and J.G. Supervision: S.M-L, M.G.-H, M.R F.-R. and J.G. Original Draft and visualization: M.S.-A., writing—review and editing: all the authors Funding acquisition: SML, MGH Investigation: M.S.-A. P.G. and J.G.

References

[1] A.H. Hartog, *An Introduction to Distributed Optical Fibre Sensors* (CRC Press, 2017).

[2] L.B. Liokumovich, N.A. Ushakov, O.I. Kotov, M.A. Bisyarin, and A.H. Hartog, "Fundamentals of Optical Fiber Sensing Schemes Based on Coherent Optical Time Domain Reflectometry: Signal Model under Static Fiber Conditions," J. Light. Technol. **33**(17), 3660–3671 (2015).

[3] X. Bao, and Y. Wang, "Recent Advancements in Rayleigh Scattering-Based Distributed Fiber Sensors," Adv. Devices Instrum. **2021**(March), 1–17 (2021).

[4] W. Zou, S. Yang, X. Long, and J. Chen, "Optical pulse compression reflectometry: proposal and proof-of-concept experiment," Opt. Express **23**(1), 512–522 (2015).

[5] H.F. Martins, K. Shi, B.C. Thomsen, S. Martin-Lopez, M. Gonzalez-Herraez, and S.J. Savory, "Real time dynamic strain monitoring of optical links using the backreflection of live PSK data," Opt. Express **24**(19), 22303–22317 (2016).

[6] C. Liang, Q. Bai, M. Yan, Y. Wang, H. Zhang, and B. Jin, "A Comprehensive Study of Optical Frequency Domain Reflectometry," IEEE Access **9**, 41647–41668 (2021).

[7] J. Li, J. Gan, Z. Zhang, X. Heng, C. Yang, Q. Qian, S. Xu, and Z. Yang, "High spatial resolution distributed fiber strain sensor based on phase-OFDR," Opt. Express **25**(22), 27913–27922 (2017).

[8] D. Chen, Q. Liu, and Z. He, "108-km Distributed Acoustic Sensor with 220-p ε/Hz Strain Resolution and 5-m Spatial Resolution," J. Light. Technol. **37**(18), 4462–4468 (2019).

[9] D. Arbel, and A. Eyal, "Dynamic optical frequency domain reflectometry," Opt. Express **22**(8), 8823–8830 (2014).

[10] I. Coddington, N. Newbury, and W. Swann, "Dual-comb spectroscopy," Optica **3**(4), 414–426 (2016).

[11] M. Soriano-Amat, H.F. Martins, V. Durán, L. Costa, S. Martin-Lopez, M. Gonzalez-Herraez, and M.R. Fernández-Ruiz, "Time-expanded phase-sensitive optical time-domain reflectometry," Light Sci. Appl. **10**(51), 1–12 (2021).

[12] M. Soriano-Amat, H.F. Martins, S. Martin-Lopez, M. Gonzalez-Herraez, M.R. Fernández-Ruiz, and V. Durán, "Time-expanded ϕOTDR using low-frequency electronics," Opt. Express **31**(2), 843–852 (2023).

[13] J. Preciado-Garbayo, M. Soriano-Amat, P. Sevillano, D. Izquierdo, H.F. Martins, S. Martin-Lopez, M. Gonzalez-Herraez, M.R. Fernández-Ruiz, and J.J. Martínez, "Time-Expanded Φ-OTDR based on binary sequences," IEEE PHOTONICS Technol. Lett. **34**(13), 695–698 (2022).

[14] N.B. Hébert, J. Genest, J.-D. Deschênes, H. Bergeron, G.Y. Chen, C. Khurmi, and D.G. Lancaster, "Self-corrected chip-based dual-comb spectrometer," Opt. Express **25**(7), 8168–8179 (2017).

[15] N.B. Hébert, V. Michaud-belleau, J. Deschênes, and J. Genest, "Self-Correction Limits in Dual-Comb Interferometry," IEEE J. Quantum Electron. **55**(4), 8700311 (1–11) (2019).

[16] K. Fdil, V. Michaud-Belleau, N.B. Hébert, P. Guay, A.J. Fleisher, J.-D. Deschênes, and J. Genest, "Dual electro-optic frequency comb spectroscopy using pseudo-random modulation," Opt. Lett. **44**(17), 4415–4418 (2019).

[17] Y. Bao, X. Yi, Z. Li, Q. Chen, J. Li, X. Fan, and X. Zhang, "A digitally generated ultrafine optical frequency comb for spectral measurements with 0.01-pm resolution and 0.7-μs response time," Light Sci. Appl. **4**(6), 1–7 (2015).

[18] K. Fdil, V. Michaud-Belleau, N.B. Hébert, and J. Genest, in *Opt. Sensors Sens. Congr.* (Optica Publishing Group, Washington, D.C., 2020), p. EM2C.4.

[19] E. Leviatan, and A. Eyal, "High resolution DAS via sinusoidal frequency scan OFDR (SFS-OFDR)," Opt. Express **23**(26), 33318–33334 (2015).

[20] L. Schenato, "A review of distributed fibre optic sensors for geo-hydrological applications," Appl. Sci. **7**(9), 896 (2017).

[21] W. Li, X. Bao, Y. Li, and L. Chen, "Differential pulse-width pair BOTDA for high spatial resolution sensing," Opt. Express **16**(26), 21616–21625 (2008).

[22] N.B. Hébert, V. Michaud-Belleau, J.D. Anstie, J.-D. Deschênes, A.N. Luiten, and J. Genest, "Self-heterodyne interference spectroscopy using a comb generated by pseudo-random modulation," Opt. Express **23**(21), 27806–27818 (2015).

[23] M. Soriano-Amat, H.F. Martins, V. Durán, S. Martin-Lopez, M. Gonzalez-Herraez, and M.R. Fernández-Ruiz, "Quadratic phase coding for SNR improvement in time-expanded phase-sensitive OTDR," Opt. Lett. **46**(17), 4406–4409 (2021).

[24] V. Durán, P.A. Andrekson, and V. Torres-Company, "Electro-optic dual-comb interferometry over 40 nm bandwidth," Opt. Lett. **41**(18), 4190–4193 (2016).

[25] M. Yan, P.L. Luo, K. Iwakuni, G. Millot, T.W. Hänsch, and N. Picqué, "Mid-infrared dual-comb spectroscopy with electro-optic modulators," Light Sci. Appl. **6**(10), 1–8 (2017).

[26] G. Tu, M. Zhao, Z. Tang, K. Qian, and B. Yu, "Fading Noise Suppression in Φ-OTDR Based on Nearest Neighbor Analysis," J. Light. Technol. **38**(23), 6691–6698 (2020).

[27] H. Gabai, and A. Eyal, "On the sensitivity of distributed acoustic sensing," Opt. Lett. **41**(24), 5648–5651 (2016).

References (extended version)

[1] A.H. Hartog, *An Introduction to Distributed Optical Fibre Sensors* (CRC Press, 2017).

[2] L.B. Liokumovich, N.A. Ushakov, O.I. Kotov, M.A. Bisyarin, and A.H. Hartog, "Fundamentals of Optical Fiber Sensing Schemes Based on Coherent Optical Time Domain Reflectometry: Signal Model under Static Fiber Conditions," J. Light. Technol. **33**(17), 3660–3671 (2015).

[3] X. Bao, and Y. Wang, "Recent Advancements in Rayleigh Scattering-Based Distributed Fiber Sensors," Adv. Devices Instrum. **2021**(March), 1–17 (2021).

[4] W. Zou, S. Yang, X. Long, and J. Chen, "Optical pulse compression reflectometry: proposal and proof-of-concept experiment," Opt. Express **23**(1), 512–522 (2015).

[5] H.F. Martins, K. Shi, B.C. Thomsen, S. Martin-Lopez, M. Gonzalez-Herraez, and S.J. Savory, "Real time dynamic strain monitoring of optical links using the backreflection of live PSK data," Opt. Express **24**(19), 22303–22317 (2016).

[6] C. Liang, Q. Bai, M. Yan, Y. Wang, H. Zhang, and B. Jin, "A Comprehensive Study of Optical Frequency Domain Reflectometry," IEEE Access **9**, 41647–41668 (2021).

[7] J. Li, J. Gan, Z. Zhang, X. Heng, C. Yang, Q. Qian, S. Xu, and Z. Yang, "High spatial resolution distributed fiber strain sensor based on phase-OFDR," Opt. Express **25**(22), 27913–27922 (2017).

[8] D. Chen, Q. Liu, and Z. He, "108-km Distributed Acoustic Sensor with 220-p ∈/Hz Strain Resolution and 5-m Spatial Resolution," J. Light. Technol. **37**(18), 4462–4468 (2019).

[9] D. Arbel, and A. Eyal, "Dynamic optical frequency domain reflectometry," Opt. Express **22**(8), 8823–8830 (2014).

[10] I. Coddington, N. Newbury, and W. Swann, "Dual-comb spectroscopy," Optica **3**(4), 414–426 (2016).

[11] M. Soriano-Amat, H.F. Martins, V. Durán, L. Costa, S. Martin-Lopez, M. Gonzalez-Herraez, and M.R. Fernández-Ruiz, "Time-expanded phase-sensitive optical time-domain reflectometry," Light Sci. Appl. **10**(51), 1–12 (2021).

[12] M. Soriano-Amat, H.F. Martins, S. Martin-Lopez, M. Gonzalez-Herraez, M.R. Fernández-Ruiz, and V. Durán, "Time-expanded φOTDR using low-frequency electronics," Opt. Express **31**(2), 843–852 (2023).

[13] J. Preciado-Garbayo, M. Soriano-Amat, P. Sevillano, D. Izquierdo, H.F. Martins, S. Martin-Lopez, M. Gonzalez-Herraez, M.R. Fernández-Ruiz, and J.J. Martínez, "Time-Expanded Φ-OTDR based on binary sequences," IEEE PHOTONICS Technol. Lett. **34**(13), 695–698 (2022).

[14] N.B. Hébert, J. Genest, J.-D. Deschênes, H. Bergeron, G.Y. Chen, C. Khurmi, and D.G. Lancaster, "Self-corrected chip-based dual-comb spectrometer," Opt. Express **25**(7), 8168–8179 (2017).

[15] N.B. Hébert, V. Michaud-belleau, J. Deschênes, and J. Genest, "Self-Correction Limits in Dual-Comb Interferometry," IEEE J. Quantum Electron. **55**(4), 8700311 (1–11) (2019).

[16] K. Fdil, V. Michaud-Belleau, N.B. Hébert, P. Guay, A.J. Fleisher, J.-D. Deschênes, and J. Genest, "Dual electro-optic frequency comb spectroscopy using pseudo-random modulation," Opt. Lett. **44**(17), 4415–4418 (2019).

[17] Y. Bao, X. Yi, Z. Li, Q. Chen, J. Li, X. Fan, and X. Zhang, "A digitally generated ultrafine optical frequency comb for spectral measurements with 0.01-pm resolution and 0.7-μs response time," Light Sci. Appl. **4**(6), 1–7 (2015).

[18] K. Fdil, V. Michaud-Belleau, N.B. Hébert, and J. Genest, in *Opt. Sensors Sens. Congr.* (Optica Publishing Group, Washington, D.C., 2020), p. EM2C.4.

[19] E. Leviatan, and A. Eyal, "High resolution DAS via sinusoidal frequency scan OFDR (SFS-OFDR)," Opt. Express **23**(26), 33318–33334 (2015).

[20] L. Schenato, "A review of distributed fibre optic sensors for geo-hydrological applications," Appl. Sci. **7**(9), 896 (2017).

[21] W. Li, X. Bao, Y. Li, and L. Chen, "Differential pulse-width pair BOTDA for high spatial resolution sensing," Opt. Express **16**(26), 21616–21625 (2008).

[22] N.B. Hébert, V. Michaud-Belleau, J.D. Anstie, J.-D. Deschênes, A.N. Luiten, and J. Genest, "Self-heterodyne interference spectroscopy using a comb generated by pseudo-random modulation," Opt. Express **23**(21), 27806–27818 (2015).

[23] M. Soriano-Amat, H.F. Martins, V. Durán, S. Martin-Lopez, M. Gonzalez-Herraez, and M.R. Fernández-Ruiz, "Quadratic phase coding for SNR improvement in time-expanded phase-sensitive OTDR," Opt. Lett. **46**(17), 4406–4409 (2021).

[24] V. Durán, P.A. Andrekson, and V. Torres-Company, "Electro-optic dual-comb interferometry over 40 nm bandwidth," Opt. Lett. **41**(18), 4190–4193 (2016).

[25] M. Yan, P.L. Luo, K. Iwakuni, G. Millot, T.W. Hänsch, and N. Picqué, "Mid-infrared dual-comb spectroscopy with electro-optic modulators," Light Sci. Appl. **6**(10), 1–8 (2017).

[26] G. Tu, M. Zhao, Z. Tang, K. Qian, and B. Yu, "Fading Noise Suppression in Φ-OTDR Based on Nearest Neighbor Analysis," J. Light. Technol. **38**(23), 6691–6698 (2020).

[27] H. Gabai, and A. Eyal, "On the sensitivity of distributed acoustic sensing," Opt. Lett. **41**(24), 5648–5651 (2016).